View Article Online
View Journal

Chemical
Science

Accepted Manuscript

This article can be cited before page numbers have been issued, to do this please use: J. Xu, R. Chen, J. Song, S. Liu, Y. Shen and Y. Zhang, *Chem. Sci.*, 2025, DOI: 10.1039/D5SC01854D.

ROYAL SOCIETY
OF CHEMISTRY

rsc.li/chemical-science

View Article Online
DOI: 10.1039/D5SC01854D

ARTICLE

# Emerging Techniques and Scenarios of Scanning Electrochemical Microscopy for the Characterization of Electrocatalytic Reactions

Jinming Xu, Ran Chen*, Juanxian Song, Songqin Liu, Yanfei Shen, Yuanjian Zhang

Received 00th January 20xx,
Accepted 00th January 20xx

DOI: 10.1039/x0xx00000x

**Abstract** To fulfill the evergrowing energy consumption demands and the pursuit of sustainable and renewable energy, electrocatalytic reactions such as water electrocatalysis, $O_2$ reduction, $N_2$ reduction (NRR), $CO_2$ reduction ($CO_2RR$), etc., have drawn a lot of attention. Scanning electrochemical microscopy (SECM) is a powerful technique for *in-situ* surface characterization, providing critical information about the local reactivity of electrocatalysts and unveiling key information about the reaction mechanisms, which are essential for the rational design of novel electrocatalysts. There has been a growing trend of SECM-based study in electrocatalytic reactions, with a major focus on water splitting and $O_2$ reduction reactions, and relying mostly on conventional SECM techniques. Recently, novel operation modes of SECM have emerged, adding new features to the functionality of SECM and successfully expanding the scope of SECM to other electrocatalytic reactions, i.e., NRR, $NO_3^-$ reduction ($NO_3RR$), $CO_2RR$ and so on, as well as more complicated electrolysis systems, i.e. gas diffusion electrodes. In this perspective, we summarized recent progresses in the development of novel SECM techniques and recent SECM-based researches in NRR, $NO_3RR$, $CO_2RR$, and so on, where quantitative information on the reaction mechanism and catalyst reactivity were uncovered through SECM. The development of novel SECM techniques and the application of these techniques can provide new insights into the reaction mechanisms of diverse electrocatalytic reactions as well as the *in-situ* characterization of electrocatalysts, facilitating the pursuit of sustainable and renewable energy.

## Introduction

The pollution issues and greenhouse effects caused by fossil fuels as well as the ever-growing demand for energy have become a worldwide concern [1–4]. Thus, the pursuit of sustainable and renewable energy, and the utilization of this energy, has drawn lots of attention [5–10]. Electrocatalytic reactions driven by electricity generated through wind power, tidal power, solar power, etc., play crucial roles in the field of sustainable and renewable energy generation and utilization [11–14]. For example, water electrolysis reaction, one of the most-studied electrocatalytic reactions, is vital for hydrogen power generation [15–17]. Carbon dioxide reduction reaction ($CO_2RR$) can convert $CO_2$ in the atmosphere into organic products [18–20]. Nitrate reduction reaction ($NO_3RR$) helps to convert the nitrogen pollutant in industrial and agriculture wastewater into value-added ammonia product [21–23]. As a result, several core electrocatalytic reactions have triggered a great deal of research [24–28].

A comprehensive knowledge of various complicated processes at the catalyst interface during an electrocatalytic reaction, including the adsorption and desorption process, the electron transfer process, solvation and desolvation behaviors, electrostatic interactions, etc., is crucial for the engineering and optimization of electrocatalytic systems as well as for the rational design of novel electrocatalysts. The structural and chemical characteristics of electrocatalysts can be examined using various characterization methods, including scanning electron microscopy-energy dispersive X-ray spectrometer (SEMEDS), X-ray photoelectron spectroscopy (XPS), UV-vis fluorescence microscopy, Raman spectroscopy and so on [29]. On the other hand, conventional electrochemical techniques such as cyclic voltammetry (CV) and electrochemical impedance spectroscopy (EIS) are widely used in the study of electrocatalytic reactions, capturing the average electrochemical properties of the catalysts [30,31]. However, since electrocatalysts are often spatially heterogeneous due to surface features at the microscopic level, i.e., surface defects, various crystalline facets and phases, non-uniform catalyst distribution, etc.[32–35], an electrochemical technique with high spatial resolution is critical for characterizing the local reactivity at different microscopic regions and unraveling the complicated reaction processes during electrolysis.

Scanning electrochemical microscopy (SECM) is a powerful and versatile technique for *in-situ* surface characterization with high spatial and temporal resolution [36–39]. Using nanoelectrodes as the probe, a lateral spatial resolution ~10 nm and a horizontal tip-substrate distance of a few nanometers on flat substrates have been achieved, enabling the detection of short-lived intermediates and the analysis of ultrafast reaction kinetics near the substrate [40–43]. Due to its high spatial resolution, *in-situ* operation modes, and versatile functionality, SECM has also been widely used in various fields, such

---

*Jiangsu Province Key Laboratory of Critical Care Medicine, Jiangsu Engineering Laboratory of Smart Carbon-Rich Materials and Device. Jiangsu Province Hi-Tech Key Laboratory for Bio-Medical Research, School of Chemistry and Chemical Engineering, Southeast University, Nanjing, 211189, China.*
*Email: rchen@seu.edu.cn*

View Article Online
DOI: 10.1039/D5SC01854D

as studying complicated reaction mechanisms, characterizing the local morphology and reactivity at the electrode surface, probing cellular activity, etc [36, 44–48]. There is a growing trend of SECM-based study in electrocatalytic reactions, where critical information on the local reactivity at different microscopic regions on an electrocatalytic material was revealed using SECM [43,49,50]. The majority of these work focused on water splitting and $O_2$ reduction reactions [51–60], and traditional SECM operation techniques, namely, the feedback mode and the generation/collection mode, were used to quantify the localized reactivity [61–63]. Additionally, since a flat electrode surface was required for positioning the probe close and carrying out accurate SECM measurements, these SECM-based studies were often limited to two-dimensional planar materials [64,65].

Recently, novel operation modes of SECM have emerged, adding new features to the functionality of SECM [66–72]. For example, the surface interrogation mode enabled the quantification of active sites on catalytic surfaces [66,67], sequential voltammetric SECM (SV-SECM) permit the simultaneous identification of numerous species in a complicated working condition and provided the capability for mapping facet-dependent products selectively [68], while shear-force-based and capacitance-based approach curves allowed for the positioning of probes near non-flat surfaces [69–72]. These new techniques helped to expand the scope of SECM to other electrocatalytic reactions, i.e., $N_2$ reduction reaction (NRR), $NO_3$RR, $CO_2$RR, and so on, as well as more complicated electrolysis systems, such as the gas diffusion electrode (GDE). Thus, in this perspective, the recent development of novel SECM techniques was first summarized, followed by the recent SECM-based research in NRR, $NO_3$RR, $CO_2$RR, and so on, where quantitative information on the reaction mechanism and catalyst reactivity were uncovered through SECM.

## Recent progress in novel SECM operative modes

### Surface interrogation mode

Although first introduced in 2008 [73,74], the surface interrogation (SI) mode of SECM has regained a lot of interest in the field of electrocatalysis recently [59,66,75,76], as it allowed for the study of active site densities and reaction kinetics where adsorbents are involved.

The working principle of the SI mode is shown in Figs. 1a-d. An UME serves as the probe to 'interrogate' the substrate surface coated with electrocatalysts by electrochemical titration. A redox mediator O is dispersed in solution, which can be reduced to R through a simple electron transfer reaction $O + e \rightarrow R$ at the biased UME surface, and when the substrate is under open circuit potential (OCP), R cannot convert back to O on the substrate. However, with the species A adsorbed at the active sites on the electrocatalyst surface, R can react with A to regenerate O, leading to a feedback current on UME, until all of the A species have reacted with R (Fig. 1b) [77]. This way, the amount of A on the electrocatalyst surface can be electrochemically titrated by monitoring the feedback current on the UME, leading to a quantification of the active site density on the electrocatalyst surface. Additionally, if there are other competing processes on the active sites, such as the adsorption of another species B (Fig. 1c), the surface concentration of A will change with time. By varying the delay time before the titration, the time-dependent surface concentration of A can be quantified, leading to kinetic information of the adsorption rate of B (Fig. 1d). Note that, a substrate comparable in size to the UME is usually required for accurate measurement of adsorbates to minimize the possible interference from lateral charge transfer effects.

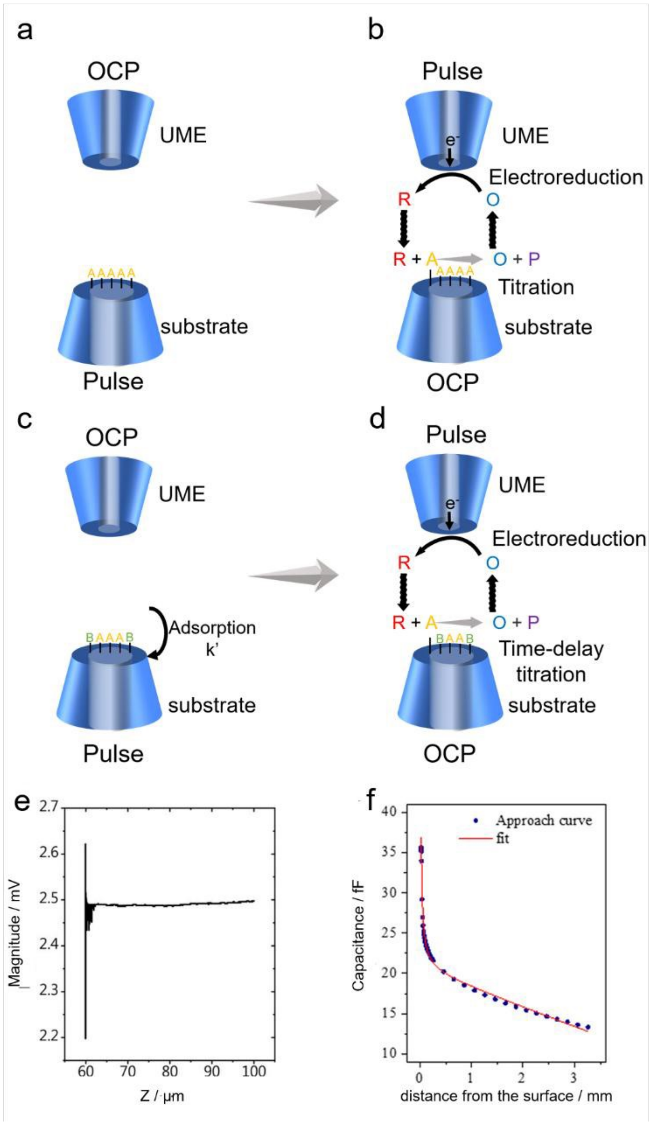

**Fig. 1** (a-d) Schematic diagrams of SECM operation modes of SI mode. P represents the byproduct of the reaction between R and A. B is a substance that competes with A for adsorption on the substrate. (e) Shear forced based approach curve. Reproduced with permission from ref. 69, Royal Society of Chemistry, 2021. (f) Capacitive approach curve obtained (blue circles) with its fit to theoretical result (red line). Reproduced with permission from ref. 71, American Chemical Society, 2019.

### Novel principles for carrying out approach curves

Prior to SECM measurements, the SECM probe (also known as the tip) was positioned near the substrate surface through the approach curve. Conventionally, the approach curve relies on the

View Article Online
DOI: 10.1039/D5SC01854D

feedback effect where the diffusion towards the tip is interfered by the substrate as the tip-substrate distance gets short, i.e. around the same magnitude as the size of the tip. The conventional approach curves prefer substrates with superior flatness, and are conducted in the aqueous phase, limiting the application of SECM when a rough substrate coated with catalysts or a solid/gas interface is under investigation. Recently, new principles for carrying out the approach curves have been proposed that address the above issues [69–72], namely the shear-force-based and the capacitance-based approach curves.

Shear force, a type of short-range hydrodynamic forces that exist only a few hundred nanometers away from solid surfaces [78], lays the foundation for shear-force-based approach curves. During the shear-force-based approach curves, a resonantly oscillating tip is moving towards the substrate by a piezo with the oscillating magnitude monitored. When far from the substrate, the oscillating magnitude on the tip barely changes, yet once the tip-substrate distance is within the range of the shear force, the oscillation characteristics of the tip are modulated by the force, indicating a successful approach to the substrate (Fig. 1e). Since the shear-force is present regardless of the surface flatness, shear-force based approach curve could work on electrodes with non-ideal flatness.

Another alternative method to carry out approach curve relies on capacitance measurements in the air [70-72]. By applying an AC voltage (typically 10 kHz, 1.4 $V_{RMS}$) on the substrate, a capacitive current can be generated on the tip. Considering the UME near a substrate as a system with a point charge positioned in front of a parallel-plate, the tip-substrate distance-dependent capacitance can be described by Eq. (1) :

$$C_{tot}(Z) = -A_1 * \ln(d_0 - Z) + B + \left(\frac{A_2}{L_{par} + d_0 - Z}\right) \quad (1)$$

where $d_0$ is the absolute surface position, $Z$ is the position of the tip varied during the approach, $C_{tot}(Z)$ is the capacitance on the tip at position Z, $A_1$, $A_2$, and $B$ are constant parameters related to experimental conditions and electrochemical system and $L_{par}$ is the length of parallel-plate. A typical capacitance-based approach curve is shown in Fig. 1f, where the capacitive current generated on the tip is recorded as the tip approaches towards the substrate using a stepper motor. As the tip gets close to the substrate, the capacitance quickly increases, and through fitting the experimental approach curve with Eq. (1), an accurate tip-substrate distance can be extracted. Note that, the capacitance measurement is conducted in the air, thus this mode allows for the positioning of a UME towards a solid/gas interface.

## Novel SECM technique-based study of electrocatalytic reactions

### SI-SECM-based NRR study

Over the past century, the Haber-Bosch process, which contributes annually to over 90% of the world's ammonia production, has powered the chemical synthesis of ammonia and fed billions of people. Due to its heavy reliance on fossil fuels, this process actually consumes around 2% of the total anthropogenic energy and emits 400 million tons of $CO_2$ annually [79–81]. The synthesis of ammonia by electrocatalysis offers the potential to operate on renewable electricity under ambient circumstances with no carbon footprint, and has garnered lots of attention recently [82-85]. $NH_3$ synthesis through the electrochemical NRR is becoming a viable substitute for the traditional Haber-Bosch fertilizer industry [86–88]. Vast amounts of efforts have been devoted to the development of stable and effective catalysts for NRR, particularly earth-abundant non-precious transition metal (TM)-based materials such as metallic oxides, sulphides, nitrides, and carbides [89–91]. However, under acidic conditions, the abundance of protons in the solution causes an increased rivalry with hydrogen evolution process (HER), posing a problem of reaction selectivity.

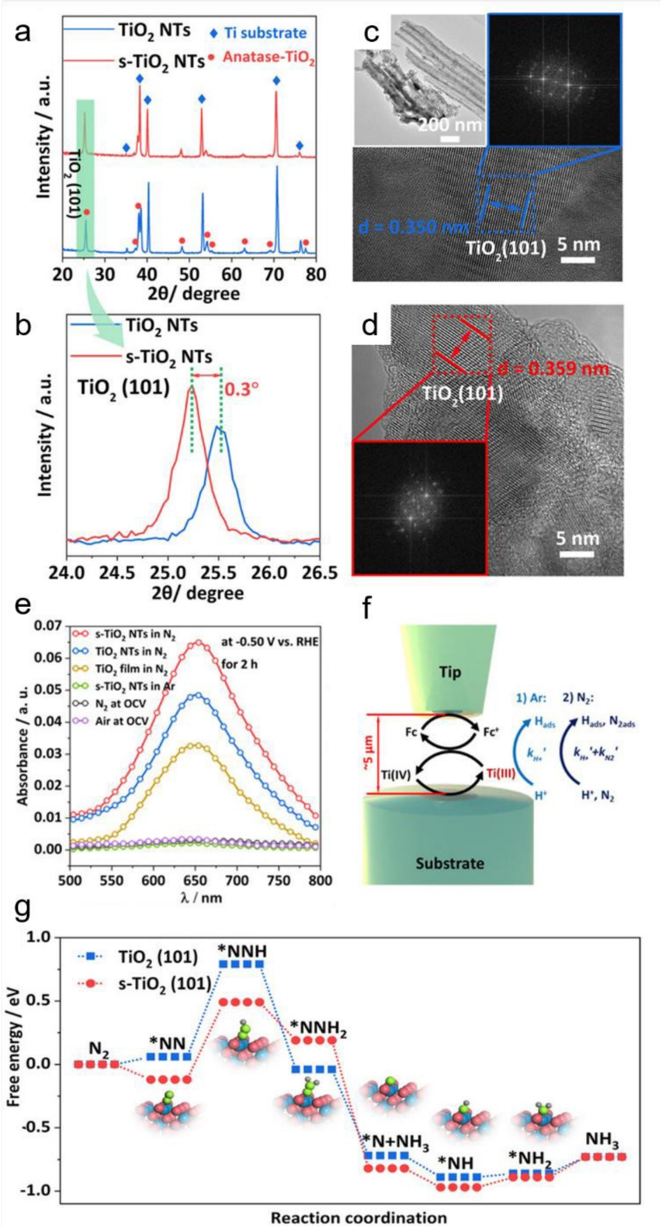

**Fig. 2** (a), (b) XRD patterns of $TiO_2$ NTs and s-$TiO_2$ NTs. (c), (d) TEM images and the corresponding fast Fourier transform (FFT) patterns (the inset) of $TiO_2$ NTs (c) and s-$TiO_2$ NTs (d). (e) UV/Vis absorption spectra of the electrolyte with indophenol indicator after 2h of electrolysis at -0.5 V. (f) Illustration of SI-SECM for determining the reaction rate constants of $H^+$ and $N_2$ adsorption on $Ti^{3+}$ site in $TiO_2$ NTs and s-$TiO_2$ NTs. (g) DFT-calculated pathways of NRR through the distal mechanisms on pristine and strained $TiO_2$ (101). Reproduced with permission from ref. 92, John Wiley and Sons, 2020.

A novel type of $TiO_2$ nanoreactor with surface strain was proposed by Li and colleagues, which allowed for the synthesis of ammonia with high selectivity [92]. $TiO_2$ nanotube arrays ($TiO_2$ NTs) were first created by anodizing Ti plates twice, followed by annealing to form anatase $TiO_2$. The electrochemical intercalation of Li ions and the follow-up delithiation created the lattice strain (s-$TiO_2$ NTs). The structural and chemical environments of $TiO_2$ nanoreactors were examined using X-ray diffraction (XRD), high-resolution transmission electron microscopy (TEM) to confirm the presence of lattice strain (Figs. 2a-d). Then the authors studied the NRR activity of the $TiO_2$ NT by applying -0.5 V on the $TiO_2$ nanoreactors for 2 hours, and monitored the $NH_3$ production through UV/vis absorption using the indophenol blue indicator. As shown in Fig. 2e, compared to $TiO_2$ NTs, the tailored s-$TiO_2$ NTs delivered improved performance for the conversion of nitrogen to ammonia. It was discovered that s-$TiO_2$ exhibited 26% higher faradaic efficiency compared to $TiO_2$ NTs. To better understand this strain-induced increase in NRR efficiency, the active site densities on $TiO_2$ and s-$TiO_2$ were quantified using the SI-SECM approach (Fig. 2f). Two identical 50 µm-diameter glass-sealed platinum UMEs served as the tip and substrate electrodes. Using a tip-generated titrant (ferrocenium, $Fc^+$), the amount of the active species, $Ti^{3+}$ on the surface of the catalyst was analyzed. More precisely, the substrate was first biased at a reduction potential $E_{\mathrm{substrate}}$ for 20 s to convert all the $Ti^{4+}$ at the active sites to $Ti^{3+}$. Then the substrate was biased at OCP, and the tip was biased to oxidize Fc to $Fc^+$, and the chronoamperometric curve on the tip was recorded. At the substrate, $Ti^{3+}$ on the catalyst surface would reduce $Fc^+$ to Fc, which was then oxidized on the tip, causing feedback current signals on the tip until all of the $Ti^{3+}$ was used up. Thus, by integrating the charges in the chronoamperometric curve, the precise amount of $Ti^{3+}$ generated at $E_{\mathrm{substrate}}$ was determined. Similarly, the reaction rate constants for the $H^+$ ($k'_{H^+}$) and $N_2$ ($k'_{N_2}$) binding on $TiO_2$ NTs and s-$TiO_2$ NTs were determined, by adding a delay time $t_d$ before the titration, and tracking the remaining $Ti^{3+}$ after $Ti^{3+}$ had reacted with $N_2$ and $H^+$ for a duration of $t_d$. The outcome indicated that both $k'_{N_2}$ and $k'_{H^+}$ exhibited characteristics of pseudo-first-order process. Specifically, $k'_{N_2}$ for s-$TiO_2$ NTs (0.62 $s^{-1}$) was almost twice that on $TiO_2$ NTs (0.32 $s^{-1}$), suggesting that $N_2$ adsorption on s-$TiO_2$ NTs was more advantageous than on $TiO_2$ NTs. Additionally, the $k'_{H^+}$ adsorption on s-$TiO_2$ was weaker compared with $k'_{N_2}$, explaining the good selectivity towards $NH_3$ production observed on s-$TiO_2$. The difference in the $k'_{N_2}$ and $k'_{H^+}$ observed on $TiO_2$ and s-$TiO_2$ was also supported by density functional theory (DFT) calculations (Fig. 2g).

Besides the SI-SECM technique, conventional SECM modes like SG/TC and SECM imaging have also been utilized in NRR study. Park et al. evaluated NRR electrocatalysis on a Fe-CuS/C electrode by *in-situ* detection of $NH_3$ using SECM for the first time [93]. Conventionally, the activity of NRR catalyst was estimated by the ex-situ detection of $NH_3$ using spectrophotometric methods including Nessler reagent, indophenol, salicylic acid reactions, etc. Additionally, liquid chromatography, ion chromatography, and rotating ring-disc electrode (RRDE) were also commonly used for ex-situ $NH_3$ detection [94]. To enable the *in-situ* detection of $NH_3$, the authors fabricated a polycrystalline Pt UME through thermochemical deposition of Pt on an unmodified Pt UME (d = 25 µm), and carried out CV measurements of the ammonia oxidation reaction (AOR) in solutions with different $NH_3$ concentration (Fig. 3a). It was found that the modified Pt UME showed an enhanced tip current towards AOR, which was due to the easier AOR kinetics and increased surface area caused by the deposited Pt nanoparticles, and a calibration curve of peak current at 0.71 $V_{RHE}$ versus $NH_3$ concentration was established (Fig. 3b). The calibration curve was compared with the ex-situ colorimetrical measurements using the indephenol method, and consistent results were obtained. Furthermore, the authors showed that the stability of NRR catalysts can be evaluated through real-time $NH_3$ detection using SECM, as presented in Fig. 3c. By locating the modified Pt UME close to the Fe-CuS/C electrode, the authors detected the $NH_3$ generated at the electrode *in-situ* and found that during repetitive CV scans, the amount of $NH_3$ produced decreased, indicating a degrading process of the Fe-CuS/C electrode (Fig. 3d).

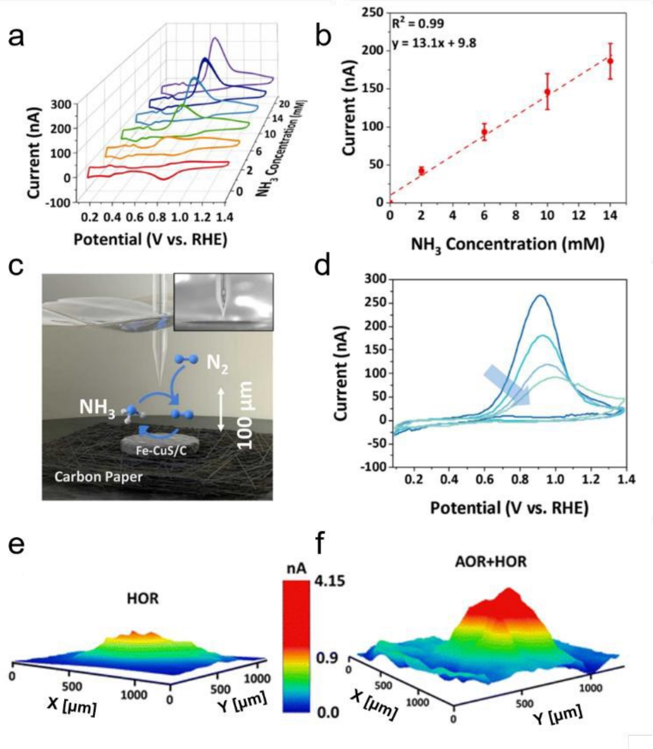

**Fig. 3** (a) CVs of $NH_3$ oxidation at the modified Pt UME in 1 M KOH solution containing 0 to 20 mM $NH_3$. Scan rate: 20 mV $s^{-1}$. (b) The relationship between $NH_3$ concentration and the peak current of

View Article Online
DOI: 10.1039/D5SC01854D

AOR in 1 M KOH solution. (c) A schematic diagram of the study of NRR on the Fe-CuS/C-loaded carbon paper with a Pt UME using the SECM SG-TC mode. The inset is an actual image of the experimental setup. (d) Repetitive CVs of AOR were collected at the Pt UME when the UME was positioned close to the Fe-CuS/C-loaded carbon paper. The carbon paper was biased at -0.2 V vs. RHE. Scan rate: 20 mV $s^{-1}$. Reproduced with permission from ref. 93, Elsevier, 2023. (e) and (f) Three-dimensional SECM image showing the local catalytic activity of $Cu-Ni_4B_3$ (1 : 2). The tip was biased at the potential of 1.1 V in (e) under Ar atmosphere to quantify HOR on the tip, and in (f) under $N_2$ atmosphere to detect the products of both HER and NRR. Reproduced with permission from ref. 95, Royal Society of Chemistry, 2023.

Nagaiah et al. prepared a $Cu-Ni_4B_3$ catalyst and investigated the competition between NRR and HER using SECM [95]. The Cu-Ni4B catalyst with a grape bunch-like morphology was synthesized by a one-step sonochemical reduction method, with Cu added to the surface of nickel boride in an effort to change the electronic structure and increase the activity of electrocatalytic NRR. Electrocatalytic NRR activity measurement with catalyst-coated glass carbon plate by chronoamperometry demonstrated that $Cu-Ni_4B_3$ (1 : 2) exhibited superior NRR activity in 0.1 M $H_2SO_4$ electrolyte compared to catalysts of other proportions. Nevertheless, the catalyst faced fierce competition from the HER in acidic environments, making it challenging to determine the absolute NRR activity using traditional ex-situ methods like gas chromatography and RRDE. In order to quantify the NRR activity of the $Cu-Ni_4B_3$ (1 : 2) catalyst and investigate the competition from HER, the *in-situ* SG/TC mode of SECM was applied (Figs. 3e and 3f). The experiments were carried out in the 0.1 M $H_2SO_4$ saturated under $N_2$ and Ar atmosphere, respectively, with 1.1 V vs. RHE applied on the tip and -0.3 V applied on the substrate. At this tip potential, both HOR and AOR could occur on the tip surface. Under Ar atmosphere, the concentration of $N_2$ in the solution was negligible, so that the current signal corresponded to the HER on $Cu-Ni_4B_3$ (1 : 2) (Fig. 3e). However, when under $N_2$ atmosphere, larger tip currents were observed, which was due to the AOR current as a result of NRR on $Cu-Ni_4B_3$ (1 : 2) (Fig. 3f), leading to a solid proof of the competition between HER and NRR.

### SI-SECM-based study of $NO_3RR$

Apart from NRR, the electroreduction of nitrate to ammonia ($NO_3RR$) has been proposed as an alternative method to synthesize $NH_3$, considering the abundant nitrate ($NO_3^-$) in waste water [96,97]. Compared to the Haber-Bosch process, $NO_3RR$ is more effective and more efficient, opening the door to waste recycling and sustainable nutrient recovery. Because of this, this approach has garnered a lot of interest, and numerous SECM-based studies have been conducted on the reaction mechanisms and selectivity of $NO_3RR$ [98–103], which also suffer from the competition from HER in a similar manner as NRR.

Yu's group constructed a new type of Cu single-atom-modified gels (Cu-SAGs) for $NO_3RR$ and nitrite-to-ammonia ($NO_2RR$) with reduced competition from HER [98]. The Cu-SAGs were synthesized through pyrolysis of the hydrogel-based precursors, namely, the supramolecularly cross-linked polypyrrole (PPy)-copper (II) phthalocyanine tetrasulfonate (CuPcTs). Afterwards, Brunauer-Emmett-Teller (BET) and scanning electron microscopy (SEM) were used to confirm the porous structure of the gel. Atomic resolution scanning transmission electron microscopy (STEM) was used to further identify the metallic substances. Afterwards, the electrochemical property of Cu-SAGs was characterized by linear sweep voltammetry (LSV). The onset potential for HER on Cu-SAGs was found to be around -0.7 V vs RHE, while the onset potential for $NO_3^-$ reduction to $NO_2^-$ and $NO_2^-$ reduction to $NH_4^+$ was found to be around -0.5 V and -0.8 V, respectively. An enhanced Faraday efficiency for $NH_3$ (~78%) over $H_2$ (~20%) was observed, with a yield rate of ~440 ug $cm^{-1}$ $h^{-1}$ for ammonia production. At more negative potentials (-0.9 V), the reduction of $NO_2^-$ to $NH_4^+$ had a faradaic efficiency close to 100%. Additionally, a noteworthy enhancement in the yield rate of $NO_2^-$ converting to $NH_4^+$ was also observed, reaching a maximum of 10.5 μg $mL^{-1}$ at -0.9 V. This value was about three times greater than that of the $NO_3RR$ under the same circumstances. These findings indicated a different path for the $NO_2RR$ with minimal influence from the HER, considerably enhancing the faradaic efficiency and yield rate. To gain insight into the mechanism of $NO_3RR$ and $NO_2RR$, the authors investigated the adsorption rate constants of $NO_3^-$, $NO_2^-$ and $H_2O$ on Cu sites using the SI-SECM technique, and discovered a much higher rate constant for $NO_2^-$ adsorption (1.98 $s^{-1}$) than that for $NO_3^-$ (0.83 $s^{-1}$) and $H_2O$ (0.06 $s^{-1}$). This result explained the enhanced activity of $NO_3^-$ reducing to $NO_2^-$ compared with HER, and it was also consistent with the molecular dynamics (MD) and DFT simulations. Based on this, a pulse electrolysis method was designed, where a higher potential of -0.5 V was first applied for 1.0 s to accumulate $NO_2^-$ near the catalyst surface to overwhelm the $H_2O$ adsorption, then a potential of -0.8 V was applied to reduce $NO_2^-$ to $NH_4^+$. Through this pulse electrolysis method, the competition from HER was heavily suppressed.

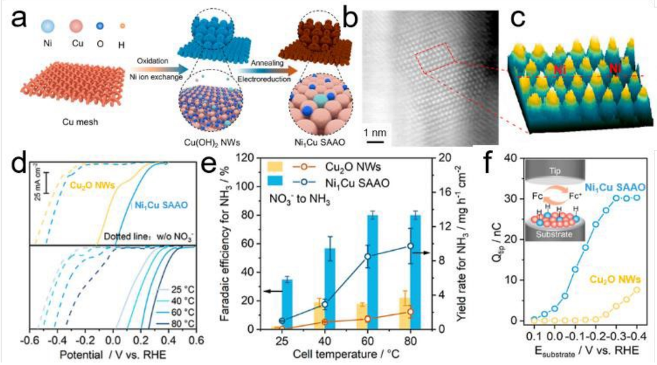

**Fig. 4** (a) Schematic representation of the $Ni_1Cu$ SAAO catalyst preparation process. (b) Atomic-resolution HAADF-STEM image of the $Ni_1Cu$ SAAO. (c) Local 3D topographic atom images for the region in (b). (d) LSVs of the $Ni_1Cu$ SAAO and $Cu_2O$ NWs with and without adding $NO_3^-$ in the electrolytes (top panel) as well as the LSVs at different cell temperatures (bottom panel). (e) Faradaic efficiency and yield rate of $Ni_1Cu$ SAAO and $Cu_2O$ NWs for the reduction of nitrate to ammonia under different cell temperatures at the

potential of 0.1 V vs RHE. (f) Plots of tip-titration charges against substrate potential using SI-SECM for quantifying the concentration of surface-active hydrogen species on $Cu_2O$ NWs and $Ni_1Cu$ SAAO in 0.01 M KOH and 1.0 mM Fc. Reproduced with permission from ref. 99, American Chemical Society, 2024.

Yu and associates created a Cu single-atom alloy oxide nanowire ($Ni_1Cu$ SAAO NW) catalyst modified with Ni-site for converting nitrate to ammonia with high efficiency [99]. $Cu(OH)_2$ nanowires were first grown on a copper mesh and then treated with a Ni ion exchange process to form $Ni_1$-$Cu(OH)_2$ NWs. The $Ni_1$-$Cu(OH)_2$ NWs were then annealed and electrochemically reduced to form the $Ni_1Cu$ SAAO (Fig. 4a), which was inspected by Aberration-corrected high-angle annular dark-field scanning TEM (AC-HAADF-STEM) to acquire a more in-depth understanding of the Ni status in $Ni_1Cu$ SAAO (Fig. 4b). A 3D topographic atom imaging analysis of the pixel intensity, as presented in Fig. 4c, made it evident that Ni atoms were located between Cu atoms and exhibited a single-atom distribution on substrate. Significantly, LSV measurements showed that compared to $Cu_2O$ NWs, the onset potential for $NO_3RR$ on $Ni_1Cu$ SAAO was substantially less negative, suggesting that $NO_3RR$ was more advantageous on the $Ni_1Cu$ SAAO catalyst (Fig. 4d). Furthermore, a clear peak of $NO_2^-$ reduction was observed at 0.1 V vs RHE in $Cu_2O$ NWs, yet this behavior was not observed on $Ni_1Cu$ SAAO. This suggested that the Ni single atoms enabled the relay electrocatalysis of $NO_2^-$ intermediate product through the Ni site-generated active hydrogen species (*H). Additionally, as the cell temperature rose, the reaction rates of both $NO_3RR$ and HER on $Ni_1Cu$ SAAO were enhanced, leading to an increase in $NH_3$ production and Faraday efficiency (Fig. 4e). This was due to the utilization of thermal energy to surmount the thermodynamic barriers in the reaction pathways. Furthermore, the reaction rate for the formation of *H on Ni single atoms was quantified through *in-situ* SI-SECM measurements to explain the increased selectivity of the $Ni_1Cu$ SAAO catalyst. More specifically, the authors used the catalyst-loaded substrate to determine the *H concentration when the $Cu_2O$ NWs and $Ni_1Cu$ SAAO were biased at different potentials. The catalytic substrate was first biased at a reducing potential $E_{substrate}$ to generate *H. After that, the system was restored to open-circuit conditions so that *H was neither generated nor consumed, and the redox reaction of the redox mediator FcMeOH (Fc) in the solution could not occur on the substrate. Then an oxidizing potential was biased on the UME to oxidize Fc to $Fc^+$. $Fc^+$ can be reduced to Fc by *H on the substrate, generating a positive feedback current on the UME until all *H were consumed by $Fc^+$, and the surface concentration of *H could be obtained from the charges transferred during the process. As $E_{substrate}$ became more negative in the first step, more *H were generated on the substrate (Fig. 4f). Remarkably, the concentration of *H on the $Ni_1Cu$ SAAO catalyst was four times greater than that on $Cu_2O$ NWs when $E_{substrate}$ was -0.4 V vs RHE. Moreover, *H production signals were seen in the $Ni_1Cu$ SAAO at a more positive potential of around 0.05 V vs RHE, indicating a considerable increase in water dissociation upon the addition of Ni single atoms. These results were also supported by the results of DFT calculations and *in-situ* Raman spectroscopy, confirming that the addition of single-atom Ni sites greatly increases the hydrogen adsorption capacitance of the $Ni_1Cu$ SAAO.

View Article Online
DOI: 10.1039/D5SC01854D

**SECM-based study of $CO_2RR$ using alternative approach curves**

One environmentally friendly way to achieve the goal of carbon neutrality is the electrochemical reduction of $CO_2$ ($CO_2RR$) into chemicals with added value using electricity from renewable sources. This process also addresses the intermittent nature of renewable electricity generation [104–108]. An additional benefit is that the electrochemical $CO_2$ reduction process operates at room temperature and pressure and may be adjusted by varying the applied potential [109], making the reaction conditions environmentally friendly. These factors enable the use of this technology in scale-up applications. SECM has been widely used in the field of CO2RR at present [68,69,72,110-112], and alternative approach curves played crucial roles in these studies where the conventional approach curves fell short.

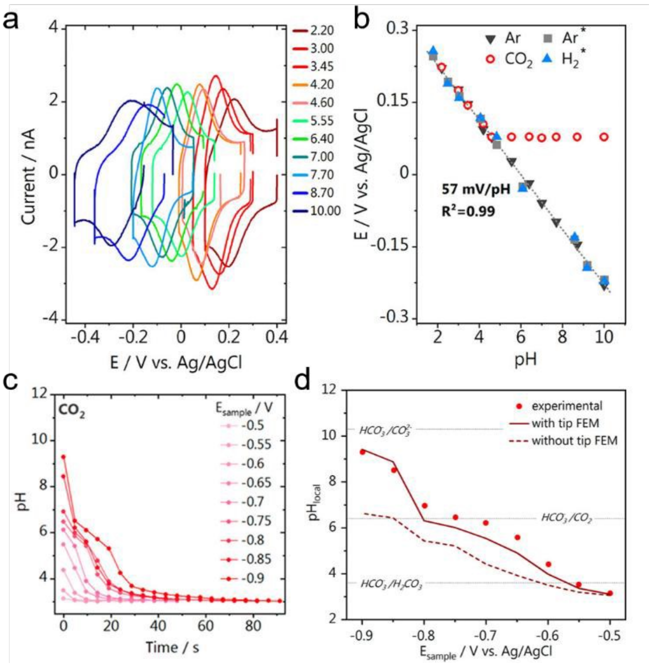

**Fig. 5** (a) CVs on the Au-UME in 0.1 M $Li_2SO_4$ solutions with different pH values. Scan rate: 200 mV $s^{-1}$. (b) Calibration curves between pH and the formal potential recorded from the Au UME pH sensor under different atmospheres. The calibration curves from previous work (grey square for Ar, blue triangle for $H_2$) are also shown for comparison. (c) The pH recovery profile recorded on the Au UME after $CO_2RR$ was turned "off" by setting the potential to 0 V vs Ag/AgCl. Before the $CO_2RR$ on the substrate was turned off, the substrate was biased at different sample potentials $E_{sample}$ (vs. Ag/AgCl). (d) Experimental (red dots) and simulated (red lines) local pH at the Au-UME after the substrate was biased at different $E_{sample}$ to drive $CO_2RR$. The local pH when the Au-UME was positioned close to the substrate (L = 3.4, dark red solid line) and when the Au-UME was positioned far from the substrate (L = 50, dark red dashed line) were both simulated. Bulk $CO_2$ concentration was fixed at 10 mM. L

is the normalized tip-surface separation. Reproduced with permission from ref. 69, American Chemical Society, 2021.

Recently, with the development of UME-based pH-sensors, the quantitative analysis of the local pH during $CO_2RR$ has been achieved using SECM, providing insight into the $CO_2RR$ mechanism [72,110]. For instance, Koper et al. designed a UME-based voltammetric pH sensor to measure the pH in the diffusion layer during $CO_2$ reduction through SECM [72]. The Au UME was functionalized with the 4-hydroxylaminothiophenol (4-HATP)/4-nitrosothiophenol (4-NSTP) redox couple. Since proton was involved in the redox reaction of 4-HATP/4-NSTP, according to Nernst equation, the formal potential of the redox reaction obtained from CV (Fig. 5a) had a linear relationship with pH, and the calibration curve was obtained in solutions with different pH values (Fig. 5b). Up to pH 3.45, the calibration curves under the argon and $CO_2$ atmospheres overlapped, while the calibration curve under $CO_2$ atmosphere reached a plateau at higher pH. This was due to the formation of $CO_2$-saturated solutions under $CO_2$ atmosphere, with a stable pH of about 4. To position the Au UME near the electrode surface, the capacitance-based approach curve was applied, and the Au UME was positioned at 80 ± 2 µm from the surface of a polycrystalline gold disc. The local pH during $CO_2RR$ was measured using tip voltammetry at 4 s/data point while the reaction on the gold disc electrode was switched 'on' and 'off' by stepping the potential from -0.5 to -0.9 V vs. Ag/AgCl in 50 mV steps, with a potential of 0 V applied during potential steps. The authors focused on the interfacial pH recovery profile once the reaction was turned 'off' by stepping the potential on gold disc back to 0 V (Fig. 5c), where no electrochemical reactions occurred. The monitored pH recovery was heavily affected by the hindered diffusion of $OH^-$ with an UME positioned in the diffusion layer, as illustrated in Fig. 5d. According to the finite element method (FEM) simulation, when the Au UME was positioned close to the substrate (L = 3.4, L being the tip-substrate distance), the $OH^-$ concentration at the Au UME surface was significantly higher than the case when the Au UME was positioned far from the substrate (L = 50). Additionally, a good fit between the experimental result and the simulated pH profile demonstrated that the diffusion hindrance caused by the UME was well-accounted for. Additionally, another UME-based voltammetric pH-sensor was used as the SECM probe to detect the local pH changes during $CO_2RR$ from the $Cu_xO_yC_z$ nanostructured electrocatalysts [110]. A Pt UME (diameter < 1 µm) was positioned to ~100 nm from the $Cu_xO_yC_z$ -coated GDE surface by the shear-force-based SECM approach curve, and the local $OH^-$ concentration near the catalyst surface was monitored as the formal potential of the redox reaction of Pt/PtO on the UME had a linear correlation with $OH^-$ concentration.

Monteiro et al. have devised a technique to probe the local activity of GDEs under *operando* conditions utilizing SECM and Au UME (r = 1 µm) (Fig. 6a and 6b) [69]. They examined the effects of $CO_2$ back-pressure and catalyst loading on the local activity of Au-GDEs (3 $cm^2$ in size) at various applied potentials. Catalysts were located onto GDEs with a loading gradient, so that a GDE surface with low to high catalyst-loading densities was used as the substrate, and the Au UME was positioned close to 100 nm from the GDE using the shear-force-based approach curve, which was otherwise impractical using conventional approach curves due to the surface roughness of GDE. The $CO_2RR$ activity on the GDE was probed using the SG/TC mode of SECM, where CO was produced on the GDE and oxidized at the Au UME, and by moving the Au UME laterally above the GDE, the activity at locations with different loading densities could be mapped. In order to maximize the performance of GDEs, the applied sample potential and the $CO_2$ back-pressure were adjusted simultaneously, and the interaction between catalyst loading and $CO_2$ back-pressure was assessed from the current signal on the Au UME. It was found that higher catalyst loadings lead to enhanced $CO_2RR$ activity in the presence of sufficient $CO_2$, while the situation was more complicated for the $CO_2$ back-pressure. An optimal $CO_2$ back-pressure was required to reach maximum $CO_2RR$ activity, which was dependent on the catalyst loading density. Additionally, Figs. 6c-e displayed the activity maps at various GDE potentials, with more CO generated at more negative potentials. It is worth noting that significant variations in the GDE activity over the scanned region were observed, indicating the inhomogeneity of the lateral response throughout the GDEs. This should not be caused by a variation in the catalyst loading density as the catalyst gradient was produced over a significantly larger length of the GDE (1.7 cm) than the length of the lateral scan in Figs. 6c-e (30 µm). As observed by SEM, a considerable number of larger holes existed on the surface of the GDE electrode, which might contribute to the notable variations in activity. The varying results demonstrated that, in addition to a high catalyst loading, sufficient $CO_2$ supply and a uniform distribution of GDE pores accessible to $CO_2$ were necessary to produce a three-phase reaction boundary.

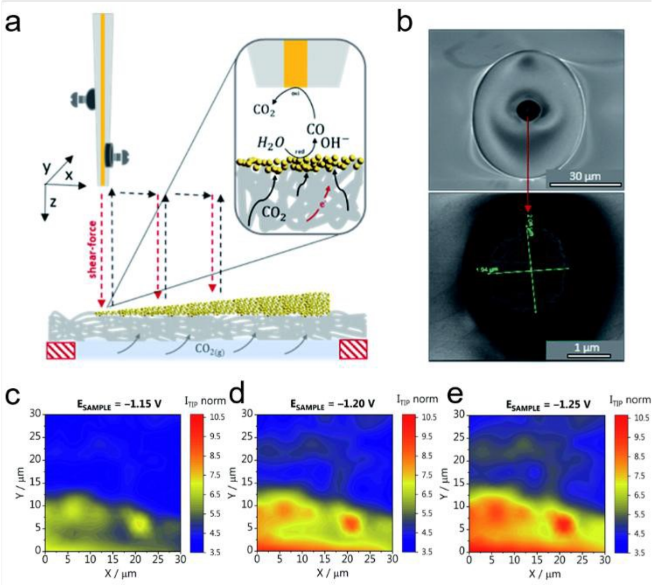

**Fig. 6** (a) Schematic representation of the SECM experimental setup, with the Au UME mounted on the piezo, approaching the GDE coated with catalysts using the capacitance-based approach curve. After the Au UME was positioned near the GDE, the $CO_2RR$ activity was characterized by the SG-TC mode, as shown in the inset. (b) SEM

micrographs of the Au UME. (c-e) Activity maps recorded for the GDE at a $CO_2$ back-pressure of 0.7 mbar. The GDE potentials were reported versus Ag/AgCl/3 M KCl in 1 M $KHCO_3$. The tip current ($I_{TIP}$ norm) was normalized to the double-layer charging current recorded at -0.6 V. Reproduced with permission from ref. 69, Royal Society of Chemistry, 2021.

Koper et al. used CV measurements to study the $CO_2RR$ on 5 mm diameter gold disc electrodes using the hanging meniscus configuration, and found that $CO_2RR$ did not occur in a pure $H_2SO_4$ electrolyte in the absence of a metal cation [111]. To confirm this and to extend the study to silver and copper electrodes, the $CO_2RR$ near the substrate with and without the presence of metal cations was monitored using the SG/TC mode of SECM with a Pt UME (r = 6.5 ± 0.07 μm) (Fig. 7a). As shown in Fig. 7b, on the gold substrate only hydrogen oxidation ($H_{2ox}$) occurred under argon atmosphere. In comparison, under $CO_2$ atmosphere, a strong peak owing to the oxidation of CO ($CO_{ox}$) appeared when $Cs^+$ was introduced to the electrolyte, while this peak was not observed in the absence of $Cs^+$. Similar outcomes were observed on silver and copper electrodes, where $CO_2RR$ occurred only in the presence of $Cs^+$ under $CO_2$ atmosphere (Fig. 7c and d). In conclusion, on gold, silver, or copper electrodes, CO was only identified under $CO_2$ atmosphere, and only after the electrolyte had been supplemented with $Cs^+$. Through DFT calculations, the authors found that $Cs^+$, as well as other alkaline metal ions, were partially desolvated in the Au-$H_2O$-$M^+$ system ($M^+$ being the metal ion), and had three promotional effects for $CO_2RR$. Namely, the existence of $Cs^+$ helped stabilize the $CO_2$ adsorption on the catalyst through the electrostatic interaction between $Cs^+$ and an oxygen atom in $CO_2$. The partially desolvated $Cs^+$ also decreased the O-C-O angle from 180 ° to 140 °, activating the $CO_2$ molecule. Lastly, the partially desolvated $Cs^+$ enhanced the electron transfer from the catalytic surface to $CO_2$. Overall, using CV and SECM, the authors demonstrated that positively charged species from the electrolyte were essential for $CO_2RR$, and the underlying mechanism was explained by DFT calculations.

View Article Online
DOI: 10.1039/D5SC01854D

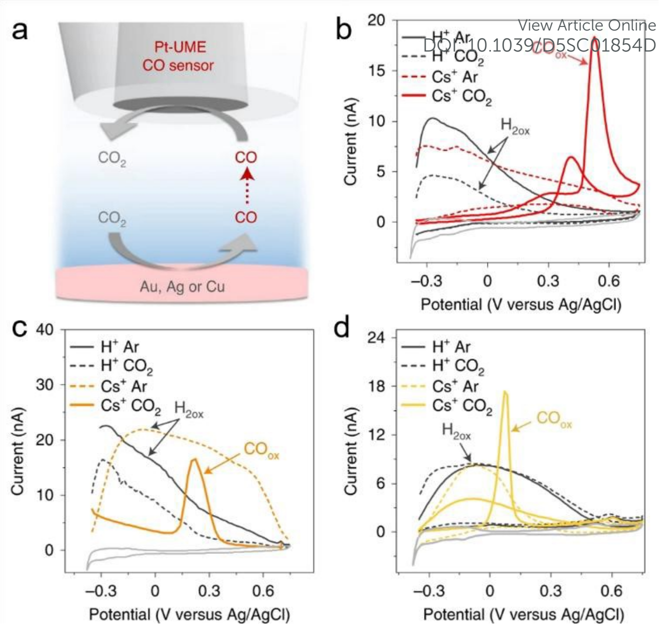

**Fig. 7** (a) Schematic representation of the SECM experiment. (b) CV on the Pt UME taken directly after $CO_2$ reduction on gold electrodes. (c) CV on the Pt UME taken directly after $CO_2$ reduction on silver electrodes. (d) CV on the Pt UME taken directly after $CO_2$ reduction on copper electrodes. The CVs on the Pt-UME before applying any potential to the sample are shown in light grey for reference. Reproduced with permission from ref. 111, Nature, 2021.

### SECM-based detection of short-lived reactive oxygen species

Reactive oxygen species (ROS) refer to a group of chemically active substances containing oxygen atoms [113-116], including singlet oxygen ($^1O_2$), hydrogen peroxide ($H_2O_2$), hydroxyl radicals (•OH), and superoxide anion radicals ($O_2$•$^-$). ROS participate in a variety of chemical and biological processes, such as energy metabolism, cell signalling, and antioxidant defence [117,118]. Nonetheless, detection of certain ROS species, such as $^1O_2$, •OH, and $O_2$•$^-$ remains challenging due to their short lifetime and high reactivity [119-129].

Known for its high reactivity, strong oxidative property, and short lifetime, it is challenging to detect •OH. Traditionally, •OH can be detected using electron spin resonance (ESR) with the help of spin traps such as 5,5-dimethyl-1-pyrroline N-oxide (DMPO), yet this method suffers from an unsatisfactory sensitivity and is inconvenient to measure the generation process of •OH in real time. To solve these issues, Rodríguez-López's group proposed a novel method for detecting •OH at operating electrodes [123]. The authors discovered that the [DMPO-OH]• adduct, formed by the reaction of •OH with DMPO, was stable in the aqueous solution and was redox-active with a formal potential of 0.85 V vs Ag/AgCl. Electrodes of various materials were tested to electrochemically generate •OH and the boron-doped diamond (BDD) was found to be the most effective one. Thus, using SECM, the freshly generated [DMPO-OH]• adduct from a BDD electrode surface was detected with a UME (12.5 μm in radius) positioned 10 μm from the BDD electrode using SECM (Fig. 8a).

View Article Online
DOI: 10.1039/D5SC01854D

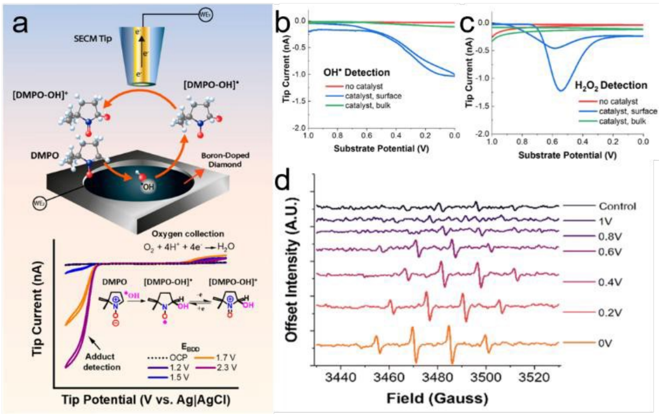

**Fig. 8** (a) Detection of the [DMPO-OH]• adduct formed from spin trapping of •OH radicals generated on BDD electrodes at different applied potentials ($E_{BDD}$) using SECM. Reproduced with permission from ref. 123, American Chemical Society, 2022. (b) The radical detection response collected at the gold tip as the substrate potential was swept at 10 mV $s^{-1}$ with 25 mM DMPO in solution. (c) The $H_2O_2$ detection response collected at a Pt tip as the substrate potential was swept at 10 mV $s^{-1}$. (d) ESR spectra of 50mM DMPO after two minutes of electrolysis at the pyrolyzed Fe-N-C catalyst substrate at increasingly reducing potentials. Reproduced with permission from ref. 130, Royal Society of Chemistry, 2024.

Furthermore, Rodríguez-López group studied ROS formation from a Fe-N-C catalyst during the ORR in real-time using the SG/TC mode of SECM [130]. Specifically, the [DMPO-OH]• adduct generated near the Fe-N-C catalyst was detected using Au UMEs with a diameter of 25 µm at a tip-substrate distance of approximately 10 µm, while $H_2O_2$ generated near the catalysts was collected using Pt UMEs (d = 25 µm). As the substrate was biased at more and more negative potentials, more OH• was generated, yet $H_2O_2$ production reached a peak when the substrate was biased at ~ 0.55 V vs. Ag/AgCl (Fig. 8b and 8c). The different behaviors of OH• and $H_2O_2$ with varying substrate potential were due to OH• being the predominant radical species, as confirmed by ex-situ ESR measurements (Fig. 8d). Overall, real-time measurements of difficult-to-observe free radical intermediates and by-products using SECM were helpful in identifying the mechanistic variations among various electrocatalytic materials for the ORR and other processes.

## Conclusions and outlook

In this perspective, the recent advances in the development of SECM operation modes were summarized. Using the shear-force-based and capacitance-based approach curves, SECM tips could be positioned near the surface of non-flat electrodes, benefiting the characterization of catalysts under operating conditions. The SI-SECM technique proves to be a powerful tool for detecting the surface active site densities, as well as determining the reaction rates of the surface adsorption process. Also, the development of potentiometric SECM probes opens up the opportunity to study local pH near the substrate at the microscopic level. All of these expanded the functionality of SECM, and SECM-based progress has been made in new scenarios, such as electrocatalytic reactions including $NO_3$RR, NRR, $CO_2$RR and so on, quantifying the catalytic properties of the catalysts and providing insights into the reaction mechanisms.

Despite recent advancements in SECM-based studies of electrocatalytic reactions, critical challenges persist in achieving quantitative kinetic information and unveiling the reaction mechanisms. The first issue is obtaining a precise tip-substrate distance when the substrate is not ideally flat, which is often the case when the substrate is loaded with nanoparticles of electrocatalysts. In SECM studies, the mass transfer towards the tip is greatly controlled by the tip-substrate distance. Thus, the current signal on the tip during SG/TC modes is not only a function of the reaction kinetics, but also largely affected by the tip-substrate distance. A precise and quantitative control of the tip-substrate distance is crucial for the quantitative study of catalytic reaction kinetics. When the substrate is flat, the tip-substrate distance can be well-controlled by comparing the approach curves with the theory, yet the approach curve over a non-flat surface such as GDE is much more complicated and usually can not be analyzed quantitatively. Even though UMEs could be brought to a few hundred nanometers above a rough substrate using the shear-force-based approach curves, a quantitative tip-substrate distance is missing, making the analysis of reaction kinetics difficult.

The second issue is the spatial resolution, which is limited by the UMEs. Although smaller UMEs have been developed, a large amount of work still prefers UMEs with 10-25 μm diameter so far. Typically, the electrocatalysts of tens to hundreds of nanometers in size were used, which were far beyond the spatial resolution provided by these UMEs. Usually, a smaller probe size leads to a better spatial resolution. However, experiments with smaller UMEs get much more challenging, and special care must be taken to properly handle the tip and the potentiostat [131,132], as well as to minimize thermal drift caused by temperature fluctuations near the tip [133].

The third challenge arises from the complicated mechanisms of multi-electron transfer reactions, including NRR, $NO_3$RR, and $CO_2$RR. These processes involve intertwined proton-coupled electron transfer (PCET) steps, competitive adsorption of intermediates, and potential-dependent selectivity bifurcations, and have multiple potential products. A lot of effort is required to acquire the selectivity towards different reaction pathways and the kinetics of each step. Moreover, the adsorption processes may play critical roles in these reactions. Using SECM, complicated reaction mechanisms involving adsorption and multiple electron transfer steps have been unveiled [134], yet the adsorption process is barely considered in current SECM-based electrocatalysis studies.

The further development of SECM-related theories, the instrumental innovation and coupling SECM with other analytical methods would be helpful to tackle these challenges. Finite element simulation combined with machine learning might help to provide a numerical solution to the theoretical approach curve over a non-flat

View Article Online
DOI: 10.1039/D5SC01854D

substrate, enabling a quantitative positioning of UME on *operando* electrodes like GDE. Multiscale modeling combining DFT-calculation, finite element simulations of intermediate surface concentration, and microkinetic analysis of PCET steps would shed light on the complicated reaction mechanisms during multi-electron transfer reactions like NRR, $NO_3RR$, and $CO_2RR$. The development of smaller UMEs as well as protocols of using these UMEs will help to greatly improve the spatial resolution of SECM-based studies [135]. And coupling *in situ* electrochemical measurements with other analytical techniques would lead to more information about reaction mechanisms. For example, by coupling rotating disk electrode with Raman spectroscopy and infrared spectroscopy, information on the adsorption of protons on noble metals has been revealed [136,137]. Coupling CV with mass spec provided structural information of the intermediates during electron transfer reactions, and can help to identify the reaction pathways [138]. Overall, progress in the above-mentioned fields will boost our understanding of the electrocatalytic reactions and facilitate the pursuit for sustainable and renewable energy.

## Author contributions

Writing-original draft, J. X.; writing-review & editing, J. S., R. C. and Y. Z.; funding acquisition, R. C and Y. Z.; supervision, Y. S. and Y. Z.

## Conflicts of interest

There are no conflicts to declare.

## Acknowledgements

This research was founded by the National Natural Science Foundation of China (22102025 and 22174014) and the ZhiShan Young Scholar Program of Southeast University.

## References

(1) J. Lelieveld, K. Klingmüller, A. Pozzer, R. T. Burnett, A. Haines and V. Ramanathan, *Proc. Natl. Acad. Sci.*, 2019, **116**, 7192-7197.
(2) K. Kohse-Höinghaus, *Chem. Rev.*, 2023, **123**, 5139-5219.
(3) S. R. Nicholson, N. A. Rorrer, A. C. Carpenter and G. T. Beckham, *Joule*, 2021, **5**, 673-686.
(4) A. A. Lacis, G. A. Schmidt, D. Rind and R. A. Ruedy, *Science*, 2010, **330**, 356-359.
(5) J. Masa, C. Andronescu and W. Schuhmann, *Angew. Chem. Int. Ed.*, 2020, **59**, 15298-15312.
(6) C. Long, J. Han, J. Guo, C. Yang, S. Liu and Z. Tang, *Chem Catal.*, 2021, **1**, 509-522.
(7) H. Zhang, M. Zhu, O. G. Schmidt, S. Chen and K. Zhang, *Adv. Energy Sustain. Res.*, 2021, **2**, 2000090.
(8) A. Kumar, V. K. Vashistha, D. K. Das, S. Ibraheem, G. Yasin, R. Iqbal, T. A. Nguyen, R. K. Gupta and M. Rasidul Islam, *Fuel*, 2021, **304**, 121420.
(9) Y. Yang, C. R. Peltier, R. Zeng, R. Schimmenti, Q. Li, X. Huang, Z. Yan, G. Potsi, R. Selhorst, X. Lu, W. Xu, M. Tader, A. V. Soudackov, H. Zhang, M. Krumov, E. Murray, P. Xu, J. Hitt, L. Xu, H. Y. Ko, B. G. Ernst, C. Bundschu, A. Luo, D. Markovich, M. Hu, C. He, H. Wang, J. Fang, R. A. DiStasio, L. F. Kourkoutis, A. Singer, K. J. T. Noonan, L. Xiao, L. Zhuang, B. S. Pivovar, P. Zelenay, E. Herrero, J. M. Feliu, J. Suntivich, E. P. Giannelis, S. Hammes-Schiffer, T. Arias, M. Mavrikakis, T. E. Mallouk, J. D. Brock, D. A. Muller, F. J. DiSalvo, G. W. Coates and H. D. Abruña, *Chem. Rev.*, 2022, **122**, 6117-6321.
(10) C. A. Campos-Roldán, D. J. Jones, J. Rozière and S.Cavaliere, *ChemCatChem*, 2022, **14**, e202200334.
(11) G. Russo, *Nature*, 2014, **513**, 478-480.
(12) A. K. Sleiti, *Renew. Sustain. Energy Rev.,* 2017, **69**, 435-441.
(13) M. Roeb and H. Müller-Steinhagen, *Science*, 2010, **329**, 773-774.
(14) H. Zhang and J. Yan, *Joule*, 2022, **6**, 1142-1144.
(15) H. Zhao and Z. Yuan, *Adv. Energy Mater.*, 2023, **13**, 2300254.
(16) J. T. Ren, L. Chen, H. Y. Wang, W. W. Tian and Z. Y. Yuan, *Energy Environ. Sci.*, 2024, **17**, 49-113.
(17) Z. Chen, S. Yun, L. Wu, J. Zhang, X. Shi, W. Wei, Y. Liu, R. Zheng, N. Han and B. J. Ni, *Nano-Micro Lett.*, 2023, **15**, 4.
(18) T. Li, P. Wang, M. He, T. Zhang, C. Yang and Z. Li, *Coord. Chem. Rev.*, 2024, **521**, 216179.
(19) B. A. Yusuf, W. Yaseen, S. Meng, J. Xie, F. O. Fapohunda, R. Nankya, A. I. Muhammad, M. Xie and Y. Xu, *Coord. Chem. Rev.*, 2023, **492**, 215273.
(20) J. Zhang, J. Ding, Y. Liu, C. Su, H. Yang, Y. Huang, B. Liu, *Joule*, 2023, **7**, 1700-1744.
(21) H. Zhang, K. Fang, J. Yang, H. Chen, J. Ning, H. Wang and Y. Hu, *Coord. Chem. Rev.*, 2024, **506**, 215723.
(22) F. Y. Chen, A. Elgazzar, S. Pecaut, C. Qiu, Y. Feng, S. Ashokkumar, Z. Yu, C. Sellers, S. Hao, P. Zhu and H. Wang, *Nat. Catal.*, 2024, **7**, 1032-1043.
(23) Y. Xiong, Y. Wang, J. Zhou, F. Liu, F. Hao and Z. Fan, *Adv. Mater.*, 2024, **36**, 2304021.
(24) H. F. Wang, L. Chen, H. Pang, S. Kaskel and Q. Xu, *Chem. Soc. Rev.*, 2020, **49**, 1414-1448.
(25) Y. Lin, Y. Dong, X. Wang and L. Chen, *Adv. Mater.*, 2023, **35**, 2210565.
(26) S. Dey, B. Mondal, S. Chatterjee, A. Rana, S. Amanullah and A. Dey, *Nat. Rev. Chem.*, 2017, **1**, 0098.
(27) J. Li, S. U. Abbas, H. Wang, Z. Zhang and W. Hu, *Nano-Micro Lett.*, 2021, **13**, 216.
(28) X. Zhao, G. Hu, G. Chen, H. Zhang, S. Zhang and H. Wang, *Adv. Mater.*, 2021, **33**, 2207650.
(29) Z. Zhang, J. Liu, Y. Xu, C. Xie, S. Wang and X. Yao, Chem. Soc. Rev., 2024, 53, 10620-10659.
(30) P. Sebastián-Pascual and M. Escudero-Escribano, *ACS Energy Lett.*, 2020, **5**, 130-135.
(31) W. Ge, Y. Chen, Y. Fan, Y. Zhu, H. Liu, L. Song, Z. Liu, C. Lian, H. Jiang and C. Li, *J. Am. Chem. Soc.*, 2022, **144**, 6613-6622.
(32) Z. Kou, X. Li, L. Zhang, W. Zang, X. Gao and J. Wang, *Small Sci.*, 2021, **1**, 2100011.
(33) E. P. Alsaç, N. Bodappa, A. W. H. Whittingham, Y. Liu, A. D. Lazzari and R. D. L. Smith, *Chem. Phys. Rev.*, 2021, **2**, 031306.
(34) E. Fabbri, M. Nachtegaal, T. Binninger, X. Cheng, B. J. Kim, J. Durst, F. Bozza, T. Graule, R. Schäublin, L. Wiles, M. Pertoso, N. Danilovic, K. E. Ayers and T. J. Schmidt, *Nat. Mater.*, 2017, **16**, 925-931.
(35) X. Qin, S. Zhu, F. Xiao, L. Zhang and M. Shao, *ACS Energy Lett.*, 2019, **4**, 1778-1783.
(36) D. Polcari, P. Dauphin-Ducharme and J. Mauzeroll, *Chem. Rev.*, 2016, **116**, 13234-13278.
(37) M. Shen, R. Ishimatsu, J. Kim and S. Amemiya, *J. Am. Chem. Soc.*, 2012, **134**, 9856-9859.
(38) R. Chen, P. Pathirathna, R. J. Balla, J. Kim and S. Ameyiya, *Anal. Chem.*, 2024, **96**, 10765-10771.
(39) Y. Li, X. Ning, Q. Ma, D. Qin and X. Lu, *TrAC Trends Anal. Chem.*, 2016, **80**, 242-254.
(40) T. Kai, M. Zhou, S. Johnson, H. S. Ahn and A. J. Bard, *J. Am. Chem. Soc.*, 2018, **140**, 16178-16183.

View Article Online
DOI: 10.1039/D5SC01894D

(41) M. Zhou, Y. Yu, K. Hu and M. V. Mirkin, *J. Am. Chem. Soc.*, 2015, **137**, 6517-6523.

(42) T. Kai, M. Zhou, Z. Duan, G. A. Henkelman and A. J. Bard, *J. Am. Chem. Soc.*, 2017, **139**, 18552-18557.

(43) Y. Yang, Y. Xiong, R. Zeng, X. Lu, M. Krumov, X. Huang, W. Xu, H. Wang, F. J. DiSalvo, J. D. Brock, D. A. Muller and H. D. Abruña, *ACS Catal.*, 2021, **11**, 1136-1178.

(44) M. A. Bhat, N. Nioradze, J. Kim, S. Amemiya and A. J. Bard, *J. Am. Chem. Soc.*, 2017, **139**, 15891-15899.

(45) R. Chen, S. Liu and Y. Zhang, *Mater. Horizons*, 2023, **10**, 52-64.

(46) K. Barman, X. Wang, R. Jia and M. V. Mirkin, *J. Am. Chem. Soc.*, 2021, **143**, 8547-8551.

(47) J. Clausmeyer and W. Schuhmann, *TrAC Trends Anal. Chem.*, 2016, **79**, 46-59.

(48) J. Zhang, Y. Liu, Y. Li, T. Zhu, J. Qiu, F. Xu, H. Zhang and F. Li, *Small Methods*, 2016, **6**, 2200689.

(49) J. Timoshenko and B. R. Cuenya, *Chem. Rev.*, 2021, **121**, 882-961.

(50) M. Rüscher, A. Herzog, J. Timoshenko, H. S. Jeon, W. Frandsen, S. Kühl and B. R. Cuenya, *Catal. Sci. Technol.*, 2022, **12**, 3028-3043.

(51) H. J. Niu, Y. Yan, S. Jiang, T. Liu, T. Sun, W. Zhou, L. Guo and J. Li, *ACS Nano*, 2022, **16**, 11049-11058.

(52) A. Djire, X. Wang, C. Xiao, O. C. Nwamba, M. V. Mirkin and N. R. Neale, *Adv. Funct. Mater.*, 2020, **30**, 2001136.

(53) G. Li, T. Sun, H. Niu, Y. Yan, T. Liu, S. Jiang, Q. Yang, W. Zhou and L. Guo, *Adv. Funct. Mater.*, 2023, **33**, 2212514.

(54) Z. Wang, R. Liu, T. Sun, M. Li, N. Ran, D. Wang and Z. Wang, *Anal. Chem.*, 2024, **96**, 7618-7625.

(55) H. Niu, C. Huang, T. Sun, Z. Fang, X. Ke, R. Zhang, N. Ran, J. Wu, J. Liu and W. Zhou, *Angew. Chem. Int. Ed.*, 2024, **63**, e202401819.

(56) C. Iffelsberger and M. Pumera, *J. Mater. Chem. A*, 2021, **9**, 22072-22081.

(57) Z. Wang, T. Sun, C. HuangFu, S. Jiang, C. Gu, L. Jiao and Z. Wang, *Nano Res.*, 2023, **16**, 10011-10017.

(58) S. Jiang, T. Sun, C. Gu, Y. Ma, Z. Wang, D. Wang and Z. Wang, *Nano Res.*, 2023, **16**, 8902-8909.

(59) L. Lan, Y. Wu, Y. Pei, Y. Wei, T. Hu, D. Lützenkirchen-Hecht, K. Yuan and Y. Chen, *Adv. Mater.*, 2025, **37**, 2417711.

(60) S. Kaur, K. Garg and T. C. Nagaigh, *ACS Energy Lett.*, 2025, **10**, 1430-1438.

(61) J. L. Fernández and A. J. Bard, *Anal. Chem.*, 2004, **76**, 2281-2289.

(62) C. M. Sánchez-Sánchez, J. Rodríguez-López and A. J. Bard, *Anal. Chem.*, 2008, **80**, 3254-3260.

(63) B. B. Katemann, A. Schulte and W. Schuhmann, *Chem. -A Eur. J.*, 2003, **9**, 2025-2033.

(64) J. Park, J. H. Lim, J. H. Kang, J. Lim, H. W. Jang, H. Shin and S. H. Park, *J. Energy Chem.*, 2024, **91**, 155-177.

(65) T. B. Clarke, L. E. Krushinski, K. J. Vannoy, G. Colón-Quintana, K. Roy, A. Rana, C. Renault, M. L. Hill and J. E. Dick, *Chem. Rev.*, 2024, **124**, 9015-9080.

(66) Z. Jin, P. Li, Y. Meng, Z. Fang, D. Xiao and G. Yu, *Nat. Catal.*, 2021, **4**, 615-622.

(67) P. Li, Z. Jin, Z. Fang and G. Yu, *Energy Environ. Sci.*, 2021, **14**, 3522-3531.

(68) Y. Nam, S.-E. Cho, H. S. Ahn, *ACS Catal.*, 2024, **14**, 17084-17089.

(69) M. C. O. Monteiro, S. Dieckhöfer, T. Bobrowski, T. Quast, D. Pavesi, M. T. M. Koper and W. Schuhmann, *Chem. Sci.*, 2021, **12**, 15682-15690.

(70) M. C. O. Monteiro, L. Jacobse and M. T. M. Koper, *J. Phys. Chem. Lett.*, 2020, **11**, 9708-9713.

(71) M. C. O. Monteiro, L. Jacobse, T. Touzalin and M. T. M. Koper, *Anal. Chem.*, 2020, **92**, 2237-2243.

(72) M. C. O. Monteiro, A. Mirabal, L. Jacobse, K. Doblhoff-Dier, S. C. Barton and M. T. M. Koper, *JACS Au*, 2021, **1**, 1915-1924.

(73) J. Rodríguez-López, M. A. Alpuche-Avilés and A. J. Bard, *J. Am. Chem. Soc.*, 2008, **130**, 16985-16995.

(74) H. S. Ahn and A. J. Bard, *J. Am. Chem. Soc.*, 2016, **138**, 313-318.

(75) X. Tang, Y. Zhang, S. Tang, D. Lützenkirchen-Hecht, K. Yuan, Y. Chen, *ACS Catal.*, 2024, **14**, 13065-13080.

(76) W. Wu and Y. Wang, *J. Am. Chem. Soc.*, 2025, **147**, 11662-11666.

(77) J. Xu, H. Gao, F. Wang and M. Zhou, *Curr. Opin. Electrochem.*, 2023, **39**, 101299.

(78) M. Nebel, K. Eckhard, T. Erichsen, A. Schulte and W. Schuhmann, *Anal. Chem.*, 2010, **82**, 7842-7848.

(79) B. H. R. Suryanto, H.L. Du, D. Wang, J. Chen, A. N. Simonov and D. R. MacFarlane, *Nat. Catal.*, 2019, **2**, 290-296.

(80) D. R. MacFarlane, P. V. Cherepanov, J. Choi, B. H. R. Suryanto, R. Y. Hodgetts, J. M. Bakker, F. M. F. Vallana and A. N. Simonov, *Joule*, 2020, **4**, 1186-1205.

(81) J. W. Erisman, M. A. Sutton, J. Galloway, Z. Klimont, and W. Winiwarter, *Nat. Geosci.*, 2008, **1**, 636-639.

(82) G. Soloveichik, *Nat. Catal.*, 2019, **2**, 377-380.

(83) S. L. Foster, S. I. P. Bakovic, R. D. Duda, S. Maheshwari, R. D. Milton, S. D. Minteer, M. J. Janik, J. N. Renner and L. F. Greenlee, *Nat. Catal.*, 2018, **1**, 490-500.

(84) X. Xin, Q. Qu, I. E. Khalil, Y. Huang, M. Wei, J. Chen, W. Zhang, F. Huo and W. Liu, *Chin. Chem. Lett.*, 2024, **35**, 108654.

(85) J. Zhang, M. Sun, J. Ren, R. Zhang, M. Ma, Q. Xue and J. Tian, *Chin. Chem. Lett.*, 2025, **36**, 110491.

(86) C. J. M. van der Ham, M. T. M. Koper and D. G. H. Hetterscheid, *Chem. Soc. Rev.*, 2014, **43**, 5183-5191.

(87) A. J. Martín, T. Shinagawa and J. Pérez-Ramírez, *Chem*, 2019, **5**, 263-283.

(88) X. Guo, H. Du, F. Qu and J. Li, *J. Mater. Chem. A*, 2019, **7**, 3531-3543.

(89) X. Yang, B. Xu, J. G. Chen and X. Yang, *ChemSusChem*, 2023, **16**, e202201715.

(90) K. N. Dinh, Q. Liang, C. F. Du, J. Zhao, A. I. Y. Tok, H. Mao and Q. Yan, *Nano Today*, 2019, **25**, 99-121.

(91) Z. J. Huba, M. D. Donakowski and A. Epshteyn, *Chem. Mater.*, 2017, **29**, 1467-1471.

(92) P. Li, Z. Jin, Z. Fang and G. Yu, *Angew. Chem. Int. Ed.*, 2020, 59, 22610-22616.

(93) J. Kong, H. Kim and H. S. Park, *Appl. Catal. B Environ.*, 2023, **338**, 123019.

(94) M. Ferrara, M. Bevilacqua, C. Tavagnacco, F. Vizza and P. Fornasiero, *ChemCatChem*, 2020, **12**, 6205-6213.

(95) D. Gupta, A. Kafle, M. Singh, D. Dahare and T. C. Nagaiah, *J. Mater. Chem. A*, 2023, **11**, 24812-24822.

(96) G. F.Chen, Y. Yuan, H. Jiang, S. Y. Ren, L. X. Ding, L. Ma, T. Wu, J. Lu and H. Wang, *Nat. Energy*, 2020, **5**, 605-613.

(97) P. H. van Langevelde, I. Katsounaros and M. T. M. Koper, *Joule*, 2021, **5**, 290-294.

(98) P. Li, R. Li, Y. Liu, M. Xie, Z. Jin and G. Yu, *J. Am. Chem. Soc.*, 2023, **145**, 6471-6479.

(99) K. Liu, H. Li, M. Xie, P. Wang, Z. Jin, Y. Liu, M. Zhou, P. Li and G. Yu, *J. Am. Chem. Soc.*, 2024, **146**, 7779-7790.

(100) H. Li, S. Li, R. Guan, Z. Jin, D. Xiao, Y. Guo and P. Li, *ACS Catal.*, 2024, **14**, 12042-12050.

(101) P. Li, L. Liao, Z. Fang, G. Su, Z. Jin and G. Yu, *Proc. Natl. Acad. Sci.*, 2023, **120**, e2305489120.

(102) P. Li, Z. Jin, Z. Fang and G. Yu, *Energy Environ. Sci.*, 2021, **14**, 3522-3531.

(103) C. Park, M. Y. Seo, T. Kwon, J. Kim, K. M. Nam, Y. K and J. Chang, *J. Am. Chem. Soc.*, 2025, **147**, 687-700.

(104) S. Nitopi, E. Bertheussen, S. B. Scott, X. Liu, A. K. Engstfeld, S. Horch, B. Seger, I. E. L. Stephens, K. Chan, C. Hahn, J. K.

Nørskov, T. F. Jaramillo and I. Chorkendorff, *Chem. Rev.*, 2019, **119**, 7610-7672.
(105) S. Pacala and R. Socolow, *Science*, 2004, **305**, 968-972.
(106) P. D. Luna, C. Hahn, D. Higgins, S. A. Jaffer, T. F. Jaramillo and E. H. Sargent, *Science*, 2019, **364**, 6438.
(107) X. Wang, Y. Wang, L. Cui, W. Gao, X. Li, H. Liu, W. Zhou and J. Wang, *Chin. Chem. Lett.*, 2024, **35**, 110031.
(108) X. Jiang, Y. Zhao, Y. Kong, J. Sun, S. Feng, X. Lu, Q. Hu, H. Yang and C. He, *Chin. Chem. Lett.*, 2025, **36**, 109555.
(109) D. D. Zhu, J. L. Liu and S. Z. Qiao, *Adv. Mater.*, 2016, **28**, 3423-3452.
(110) N. Sikdar, J. R. C. Junqueira, S. Dieckhöfer, T. Quast, M. Braun, Y. Song, H. B. Aiyappa, S. Seisel, J. Weidner, D. Öhl, C. Andronescu and W. Schuhmann, *Angew. Chem. Int. Ed.*, 2021, **60**, 23427-23434.
(111) M. C. O. Monteiro, F. Dattila, B. Hagedoorn, R. García-Muelas, N. López and M. T. M. Koper, *Nat. Catal.*, 2021, **4**, 654-662.
(112) Y. Y. K., M. Balamurugan, K. T. Nam, B. Gopal and A. S. Kumar, *J. Mater. Chem. A*, 2024, **12**, 31135-31144.
(113) Y. Zhang, M. Dai and Z. Yuan, *Anal. Methods*, 2018, **10**, 4625-4638.
(114) J. Wu, Y. Zhao, K. Li, S. Muhammad, M. Ju, L. Liu, Y. Huang, B. Wang, W. Ding, B. Shen and H. Huang, *TrAC Trends Anal. Chem.*, 2022, **157**, 116734.
(115) F. Yan, Y. Zang, J. Sun, Z. Sun and H. Zhang, *TrAC Trends Anal. Chem.*, 2020, **131**, 116009.
(116) N. Kwon, D. Kim, K. M. K. Swamy and J. Yoon, *Coord. Chem. Rev.*, 2021, **427**, 213581.
(117) Y. Su, H. Song and Y. Lv, *Microchem. J.,* 2019, **146**, 83-97.
(118) D. Wang, L. Zhao, L. H. Guo and H. Zhang, *Anal. Chem.*, 2014, **86**, 10535-10539.
(119) W. Yu and L. Zhao, *TrAC Trends Anal. Chem.*, 2021, **136**, 116197.
(120) C. Iffelsberger, T. Raith, P. Vatsyayan, V. Vyskočil and F. M. Matysik, *Electrochim. Acta*, 2018, **281**, 494-501.
(121) X. Zhao, S. Lam, J. Jass and Z. Ding, *Electrochem. Commun.*, 2010, **12**, 773-776.
(122) F. P. Filice and Z. Ding, *Analyst*, 2019, **144**, 738-752.
(123) J. S. Barroso-Martínez, A. I. B. Romo, S. Pudar, S. T. Putnam, E. Bustos, J. Rodríguez-López, *J. Am. Chem. Soc.*, 2022, **144**, 18896-18907.
(124) A. Preet and T. E. Lin, *Catalysts*, 2021, **11**, 594.
(125) C. G. Zoski, *J. Electrochem. Soc.*, 2016, **163**, H3088-H3100.
(126) P. Bertoncello, *Energy Environ. Sci.*, 2010, **3**, 1620.
(127) J. Zhang, Y. Liu, Y. Li, T. Zhu, J. Qiu, F. Xu, H. Zhang and F. Li, *Small Methods*, 2022, **6**, 2200689.
(128) A. Latus, J. M. Noël, E. Volanschi, C. Lagrost and P. Hapiot, *Langmuir*, 2011, **27**, 11206-11211.
(129) T. Wu, X. Ning, Q. Xiong, F. Zhang and P. He, *Electrochim. Acta*, 2022, **403**, 139638.
(130) S. T. Putnam and J. Rodríguez-López, *Chem. Sci.*, 2024, **15**, 10036-10045.
(131) N. Nioradze, R. Chen, J. Kim, M. Shen, P. Santhosh and S. Amemiya, *Anal. Chem.,* 2013, **85**, 6198-62.
(132) J. Kim, B. Kim, S. K. Cho and A. J. Bard, *J. Am. Chem. Soc.*, 2014, **136**, 8173-8176.
(133) J. Kim, M. Shen, N. Nioradze and S. Amemiya, *Anal. Chem.*, 2012, **84**, 3489-3492.
(134) M. A. Bhat, N. Nioradze, J. Kim, S. Amemiya and A. J. Bard, *J. Am. Chem. Soc.*, 2017, **139**, 15891-15899.
(135) J. Kim, C. Renault, N. Nioradze, N. Arroyo-Currás, K. C. Leonard and A. J. Bard, *Anal. Chem.*, 2016, **88**, 10284-10289.
(136) S. Zhu, X. Qin, F. Xiao, S. Yang, Y. Xu, Z. Tan, J. Li, J. Yan, Q. Chen, M.Chen and S. Shao, *Nat. Catal.*, 2021, **4**, 711-718.
(137) S. Zhu, X. Qin, Y. Yao, and S. Shao, *J. Am. Chem. Soc.*, 2020, **142**, 8748-8754.
(138) X. Zhang, W. Lu, C. Ma, T. Wang, J. Zhu, R. N. Zare and Q. Min, *Chem. Sci.*, 2022, **13**, 6244-6253.

View Article Online
DOI: 10.1039/D5SC01854D

## Data Availability Statement

No primary research results, software or code have been included and no new data were generated or analysed as part of this review.